Conjugate photoelectron energy spectra derived from coincident FUV and radio measurements

J. M. Urco[1,5], F. Kamalabadi[1], U. Kamaci[1], B. J. Harding[2], H. U. Frey[2], S. B. Mende[2], J. D. Huba[3], S. L. England[4], T. J. Immel[2],

[1]Department of Electrical and Computer Engineering and Coordinated Science Laboratory, University of Illinois at Urbana-Champaign, Urbana, Illinois, USA
[2]Space Sciences Laboratory, University of California-Berkeley, Berkeley, CA
[3]Syntek Technologies, Fairfax, VA
[4]Virginia Polytechnic and State University, Blacksburg, VA
[5]Leibniz-Institute for Atmospheric Physics, University of Rostock, Kuehlungsborn, Germany

Key Points:

- Nightglow emissions excited by photoelectrons originating in the magnetically conjugate hemisphere is observed by the ICON mission
- Conjugate photoelectron energy spectra is derived for the first time using global scale far-ultraviolet and radio-occultation observations
- Comparison of estimated photoelectron fluxes with a first principle model shows consistent characteristics

Corresponding author: J. M. Urco, `mcordero@illinois.edu`

Abstract

We present a method for estimating incident photoelectrons' energy spectra as a function of altitude by combining global scale far-ultraviolet (FUV) and radio-occultation (RO) measurements. This characterization provides timely insights important for accurate interpretation of ionospheric parameters inferred from the recently launched Ionospheric Connection Explorer (ICON) observations. Quantification of photoelectron impact is enabled by the fact that conjugate photoelectrons (CPEs) directly affect FUV airglow emissions but not RO measurements. We demonstrate the technique for the estimation of photoelectron fluxes and their spectra by combining coincident ICON-FUV and COSMIC2 measurements and show that a significant fraction of ICON-FUV measurements are affected by CPEs during the winter solstice. A comparison of estimated photoelectron fluxes with the SAMI2-PE model is used to gain further insights into the estimation method and reveals consistent values at low latitudes, while the results suggest that the model might be overestimating photoelectron fluxes by ∼10% at mid latitudes.

Plain Language Summary

The impact of solar radiation on the atmosphere produces highly energetic electrons, which travel freely along the magnetic Earth's field lines from one hemisphere to the other. When these electrons flow from the sunlit side into the nightside hemisphere, they interact with the neutral species and produce noticeable effects in the ionosphere such as an increase in electron temperature and enhancement of airglow emissions. This study presents a method to quantify the amount of precipitating electrons and their energy on a global scale using two recent satellite missions (ICON and COSMIC2). Our results demonstrate that coincident far-ultraviolet (ICON) and radio-occultation (COSMIC2) measurements from space are valuable resources to study precipitating electrons in the ionosphere and their impact on inferring ionospheric plasma parameters.

1 Introduction

Photoionization of the neutral atmospheric species by extreme-ultraviolet solar radiation and X-rays produces highly energetic electrons in the ionosphere, also known as photoelectrons (PEs). Conjugate photoelectrons (CPEs) refer to those PEs that travel along the magnetic field lines from one hemisphere to the other and lose their energy through inelastic collisions with neutral particles and the ambient electrons in the local region. Such interactions result in elevation of the ambient electron's temperature (Duboin et al., 1968), additional electron production (Swartz, 1972), and enhancement of airglow emissions (Hanson, 1963; Cole, 1965; Fontheim et al., 1968; Duboin et al., 1968).

Although CPEs' effects are present during day and night, their impacts are more significant when and where the local point is in darkness and its magnetically conjugate point is not. Evidence of an increase in electron temperature by more than 100% at pre-dawn caused by CPE impact has been reported using in-situ satellite measurements (Narasinga Rao & Maier, 1970), and incoherent scatter radar (ISR) measurements (Evans, 1967; Carlson, 1966, 1968). Moreover, pre-dawn airglow enhancements at visual wavelengths have been reported by various authors (Bennett, 1969; Carman et al., 1969; Cogger & Shepherd, 1969; Smith, 1969; Christensen, 1975). At far-ultraviolet (FUV) wavelengths, Meier (1971) reported the first observations of airglow enhancement at pre-dawn using OGO-4. More recently, Solomon et al. (2020) and Kil et al. (2020) have reported pre-dawn airglow enhancements observed by GOLD (Eastes et al., 2008, 2017) and SSUSI (Paxton et al., 2017, and references therein), respectively. In both cases, regions affected by CPEs show one order of magnitude brighter airglow emissions than those not affected.

First measurements of CPE fluxes date back to Peterson et al. (1977) using the Atmosphere Explorer C, and to Shepherd et al. (1978) and Mukai et al. (1979) using sounding rockets. They found that CPEs can travel along the magnetic field lines from one hemisphere to the other without significant degradation. Furthermore, they reported that more than 65% of the 630 nm airglow emissions were produced by direct impact of PEs with atomic oxygen. Another substantial amount of PE measurements from 1996 to 2009 at ∼3500km altitude is available from the FAST satellite (Pfaff et al., 2001). Using FAST data, Richards and Peterson (2008) found that about 60% of the precipitating energy flux is backscattered to the conjugate hemisphere. Despite the existing observations, the resulting data do not provide sufficient spatial and temporal coverage to specify PE fluxes for all geophysical, temporal, and altitudinal conditions. Consequently, parameterized models have been developed and are generally used to obtain PE fluxes.

Nagy and Banks (1970) performed initial PE generation, transport, and impact calculations. Since then, various methods have been developed to model PE transport in the ionosphere such as FLIP (Richards & Torr, 1990), SUPIM (Bailey & Balan, 1996), GLOW (Solomon, 2017), and SAMI2-PE (Varney et al., 2012). Among all these numerical first-principle calculations, the multi-stream PE transport model implemented in SAMI2-PE is one of the most comprehensive and can reproduce the electron temperature and density observed by Jicamarca closely at all local times with a discrepancy on the order of $< 30\%$. Nevertheless, the high fidelity achieved by SAMI2-PE comes with a considerable computational price, and it is sensitive to the pitch angle resolution selected. Other faster method such as the two-stream electron transport implemented in GLOW (Solomon et al., 2020) has demonstrated to be good at reproducing twilight airglow emissions observed by GOLD at latitudes lower than 60°, although some discrepancies observed at mid and high latitudes were associated with the reduced number of pitch angles used, and other neglected terms such as scattering losses or meridional transport.

Besides models, several techniques have been proposed to estimate PE fluxes from measurements. Early attempts to infer PE fluxes from simultaneous measurements of the OI lines and the N2 band, and from ISR measurements using the continuity equation were described by Rees and Luckey (1974) and Semeter and Kamalabadi (2005), respectively. Although the ISR-based problem has the advantage of possessing more degrees of freedom and the capability to retrieve altitude information compared to that of optical measurements, it is still sensitive to the pitch angle distribution assumed, and its estimates are confined to a specific geographic location.

The study presented in this paper develops a method for estimating PE energy fluxes as a function of altitude on a global scale from combined FUV and radio-occultation (RO) measurements. Although this technique might be applicable to both day and nighttime data, we focus on nighttime observations since there have been numerous observations of twilight airglow enhancements at 135.6 nm due to PEs originating in the magnetically conjugate hemisphere (CPEs). In contrast to available global PE observations which do not provide altitude information (Pfaff et al., 2001), or to ISR methods which are confined to one geographic location Semeter and Kamalabadi (2005), our technique enables, for the first time, the quantification of PE fluxes globally as a function of altitude and energy. This new capability provides further insight into the energetics of the thermosphere/ionosphere, and can complement models to explain observations that cannot be reproduced precisely, e.g., airglow emissions at mid/high latitudes.

The main challenge in interpreting FUV observations independently is to separate volume emissions due to radiative recombination (RR) and mutual neutralization (MN) from that due to PE impact. We employ RO measurements to perform full RR and MN calculations and use these results to isolate the PE contribution from FUV measurements. Once the PE contribution is isolated, it is used to estimate PE fluxes. Experimental results are presented using ICON-FUV measurements combined with ROs measurements from COSMIC2. Initial validations are performed comparing the estimated PE fluxes with SAMI2-PE outputs.

2 FUV and RO measurements

2.1 ICON: FUV measurements

The Ionospheric Connection Explorer (ICON) is a NASA mission launched in October 2019 into a 27° inclination, 598km altitude circular orbit and equipped with four scientific instruments. ICON is dedicated to making continuous observations of the neutral atmospheric drivers and the resulting ionospheric responses (Immel et al., 2018).

One of the ICON's payloads is the FUV instrument, which was designed to provide disk and limb-scan images during day and nighttime (Mende et al., 2017). During nighttime, the spectrographic FUV imager onboard ICON images the limb altitude profile in the shortwave band at 135.6 nm. This band is sensitive to the OI 135.6 nm emission and also to LBH (2,0), (3,0), (4,0) and (5,2) bands in its passband (Mende et al., 2017). In this work, we only consider the influence from OI 135.6 nm, the dominant source.

To infer O+ density profiles, which in the nighttime ionosphere is approximately equal to the electron density (e.g. Kamalabadi et al., 1999, 2002, 2009; Qin et al., 2015; Kamalabadi et al., 2018), the ICON's field of view is divided into six vertical stripes, where each stripe has a horizontal and vertical resolution of 128km x 4km at 155km altitude. Each stripe is used to infer electron density profiles every 12s in its corresponding direction.

The operational forward model to infer electron density from limb viewing integrated OI 135.6 nm emissions includes the two primary mechanisms, namely, RR and MN (Qin et al., 2015; Kamalabadi et al., 2018). In this work, CPE impact as a source of OI 135.6 nm emissions is considered, which at some times and at particular locations is more important than the first two. Since the ICON's algorithm (Kamalabadi et al., 2018) did not consider this third source, here we use the volume emission rates estimated from the FUV images and combine them with COSMIC2 occulations to isolate the contribution of CPE impact.

2.2 COSMIC2: RO measurements

The Constellation Observing System for Meteorology, Ionosphere and Climate-2 (COSMIC2) is an international Taiwan-US mission consisting of six low-Earth orbiting (LEO) satellites launched in 2019 into a 24° inclination, ∼520km circular orbit (Anthes & Schreiner, 2019; W. S. Schreiner et al., 2020). The primary payload of each LEO satellite is a Tri-Global Navigation Satellite System (GNSS) RO receiver developed by NASA's Jet Propulsion Laboratory, which has GPS, GALILEO, and GLONASS tracking capability (Tien et al., 2012). GNSS satellites orbit Earth at ∼20,000km and broadcast signals at two different L-band frequencies. The RO receiver measures the phase and amplitude of GNSS radio signals as GNSS satellites are occulted by the Earth's ionosphere. Under the assumption of straight-line propagation of GNSS signals, the total electron content (TEC) along the LEO-GPS link can be calculated from the phase difference of the two received L-band signals (e.g. W. S. Schreiner et al., 1999; Kuo et al., 2004; W. Schreiner et al., 2007; Yue et al., 2013, and references therein).

Furthermore, by assuming that the electron density is spherically symmetrical, the altitudinal electron density profile is derived through recursive inversion of slant TEC (e.g. Lei et al., 2007; W. S. Schreiner et al., 1999). Particularly, COSMIC2 uses the so-called onion peeling method that calculates the electron density of discrete layers below the LEO altitude starting from the uppermost altitude, on both the ascending and descending parts (Syndergaard et al., 2005). Since the LEO satellites move as they collect the GNSS signals, the LEO-GNSS link's geographical location at the top and at the bottom altitude might differ by several hundred kilometers (up to 1500km). Therefore, horizontal ionospheric gradients may significantly affect the retrievals. Although the symmetry assumption is not always fulfilled, COSMIC2 satellites are expected to provide 5000 vertical density profiles per day with an F peak-density and peak-height within 15% and 20km accuracy, respectively (Yue et al., 2014; W. S. Schreiner et al., 2020).

3 Excitation of OI 135.6 nm nightglow emissions by conjugate photoelectrons

The two primary production mechanisms of OI 135.6 nm emissions in the nighttime ionosphere are RR of electrons with O+, and MN of O+ with O- (Meier, 1991, and references therein). Moreover, there are some times and regions when and where the magnetically conjugate point is sunlit and the local point is not. In those cases, PEs produced by photoionization in the sunlit hemisphere are transported along the magnetic field lines to the other hemisphere and excite the neutral atoms in the nightside, producing additional airglow emissions.

The global morphology of twilight airglow emissions at 130.4nm and 135.6 nm produced by CPE impact have recently been reported by Kil et al. (2020) using the SSUSI instrument onboard the Defense Meteorological Satellite Program-F16. The morphology of both OI lines was in good agreement with the distribution of CPEs, suggesting that these airglow emissions are signatures of CPEs. The distribution of CPEs is determined by the geomagnetic field configuration and solar zenith angle (SZA). The importance of using high-fidelity representations of the geomagnetic field model to accurately reproduce the twilight airglow emissions was described by Waldrop et al. (2008). Subsequently, Solomon et al. (2020) reproduced consistently the intensity and morphology of twilight emissions observed by GOLD with the GLOW model, which includes CPE transport and uses the International Geomagnetic Reference Field model.

Twilight features are primarily visible during the winter solstice, i.e., during the December solstice in the northern hemisphere and June solstice in the southern hemisphere. During other periods the terminator approximately aligns with the magnetic field lines, and therefore, areas affected by CPEs are negligible. Figure 1(a) shows disk images at 135.6 nm obtained from GOLD on January 6, 2020 at 07:21 UTC (winter solstice) similar to those shown by Solomon et al. (2020). The morning terminator's approximate location and its magnetically conjugate trace in the winter hemisphere are indicated by the solid and dashed red lines, respectively. Note that airglow emissions in the dayside are at least two orders of magnitude brighter than the nightside. Interestingly, there is an area of faint airglow emissions in the nightside near the terminator whose morphology matches perfectly with the conjugate trace. This indicates that these emissions are most likely produced by CPE impact.

Volume emission rates (VERs) at the peak height ($\sim$250km) estimated from ICON-FUV limb scans are shown in Figure 1(b). Details of the FUV measurements, the forward model, and the retrieval technique are described in (Qin et al., 2015; Kamalabadi et al., 2018). Figure 1(b) shows all the ICON-FUV estimates for January 2020 at 07:30UTC +/- 30min, which are plotted in their corresponding latitude and longitude position. Although the twilight airglow morphology changes slowly with the season, the main pattern remains and it is similar to the one observed by GOLD. Besides the airglow emission at pre-dawn, there is a faint nightglow region near the evening terminator, which also matches with its conjugate trace. Airglow emissions due to PE and RR are both present at post-dusk and pre-dawn. Therefore, contributions to the OI 135.6 nm airglow from RR, MN, and CPE impact need to be isolated to accurately interpret FUV observations at those times.

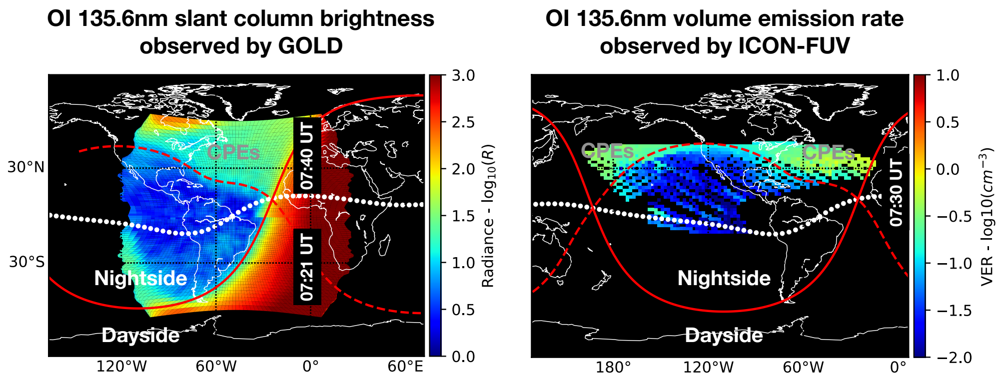

Figure 1. Airglow emissions at 135.6 nm observed by GOLD (left) and by ICON-FUV (right). Two GOLD image sequences of the OI 135.6 nm emission on January 6, 2020 at 07:21UT and 07:40UT are shown. VERs by ICON are one-hour average values around 07:30UT during January 2020. The magnetic equator is shown by white dots. The nighttime terminator at 300km altitude and its conjugate trace are shown by solid and dashed red lines, respectively. On the nightside, faint airglow emissions (green-yellowish areas) evidence CPE excitation.

4 Retrieving photoelectron energy spectra from FUV and RO measurements

To estimate the PE energy spectra, we first need to isolate emissions generated through PE impact from total airglow emissions. FUV instruments such as ICON-FUV (Mende et al., 2017) or GUVI (Christensen et al., 1994) that measure limb viewing integrated airglow emissions allow inferring the source VER of OI 135.6 nm as a function of altitude (Qin et al., 2015; Kamalabadi et al., 2018; Comberiate et al., 2007). When these emissions are affected by PEs, contributions due to RR and MN cannot be readily isolated from that due to PE impact.

The source VER ε_0 of the 135.6 nm line can be calculated by

$$\varepsilon_0(h) = \varepsilon_{rr}(h) + \varepsilon_{mn}(h) + \varepsilon_{pe}(h), \tag{1}$$

where ε_{rr}, ε_{mn}, ε_{pe} are the isotropic volume emissivities due to RR, MN, and CPE impact at a given altitude h, respectively. The first term ε_{rr} is a function of the electron density N_e and the atomic oxygen ion density [O+] (Hanson, 1969). Likewise, ε_{mn} is a function of Ne, [O+], and the atomic oxygen density [O] (Knudsen, 1970; Hanson, 1970; Tinsley et al., 1973). Since in the F region ionosphere O+ is the dominant ion species, [O+] is approximately equal to N_e. Moreover, assuming that [O] is known (e.g., from the NRL-MSISE00 model (Picone et al., 2002)), ε_{rr} and ε_{mn} can be expressed as a function of one unknown only (N_e) (Qin et al., 2015; Kamalabadi et al., 2018). This simplification allows to perform full RR and MN calculations from electron density measurements obtained by ionosondes, ISRs, or RO measurements.

When coincident FUV and RO measurements exist, ε_0 can be measured from FUV instruments onboard satellites, and ε_{rr} and ε_{mn} can be inferred from RO measurements. Therefore, an estimate of the volume excitation rate $\tilde{\varepsilon}_{pe}$ can be calculated using (1). The vast quantity of density profiles available from ICON and COSMIC2 permit the estimation of $\tilde{\varepsilon}_{pe}$ on a global scale.

4.1 Forward model

As discussed by Meier (1991), airglow emissions at 135.6 nm by PE impact occur primarily through excitation of ground-state O(^5S) atoms. The rate of excitation ε_{pe} can be expressed as a function of the PE flux by

$$\varepsilon_{pe}(h) = [O](h) \int_{E_{min}}^{E_{max}} \phi(h, E)\, \sigma(E)\, dE, \tag{2}$$

where $\sigma(E)$ (cm^{-2}) is the electron impact excitation cross section, $\phi(h, E)$ ($cm^{-2}s^{-1}eV^{-1}$) is the PE flux at altitude h and energy E, and E_{min} is the threshold energy for excitation. Typical values for E_{min} and E_{max} are 5eV and 100eV, respectively, since out of this range the excitation cross-sections for OI 135.6 nm are negligible. The model cross-sections are available from (Meier, 1991) and the atomic oxygen density [O] from the NRL-MSISE00 model (Picone et al., 2002). Thus, ε_{pe} can be expressed as a function of the PE flux only.

One common feature in models is that the precipitating electron spectra is represented by a particular distribution. A Maxwellian distribution has been used by many authors to represent thermal electrons (Varney et al., 2012) and precipitating auroral electrons (e.g. Kaeppler et al., 2015, and references therein). Other authors found that a Gaussian distribution might be more appropriate for discrete aurora (Jursa, 1985; Banks et al., 1974; Strickland et al., 1989; Khazanov et al., 2014). For highly energetic electrons, Myers et al. (1975) modeled the spectra as a slowing-down distribution and obtained a good agreement compared to those obtained from rocket measurements (Hays & Sharp, 1973). Similarly, Kondo and Ogawa (1976) and Mukai et al. (1979) used the slowing-down approximation to calculate the PE flux at the top of the atmosphere.

In the nighttime ionosphere, there is no local PE production and thus $\phi(h, E)$ represents only CPE fluxes. CPEs are exposed to different collisions before reaching their final destination and consequently their spectra is a smooth function of energy (Varney et al., 2012). Based on this, we use the slowing-down approximation to represent the CPE spectra as done by Kondo and Ogawa (1976). This distribution has the advantage of being smooth and having only two degrees of freedom (amplitude and width) compared to, for example, the Gaussian distribution, which has three degrees of freedom (amplitude, mean, and width). The slowing-down distribution is given by

$$\phi(h, E) = Q_h \exp(-E/E_h), \tag{3}$$

where $\phi(h, E)$ is a function of the characteristic flux Q_h and the characteristic energy E_h at a given altitude h. Replacing (3) in (2) results in that $\varepsilon_{pe}(h)$ is a non-linear function of Q_h and E_h.

4.2 Inversion method

Rather than solving for the electron spectra $\phi(h)$ using regularized inversion techniques (e.g., Semeter & Kamalabadi, 2005), we formulate the problem as a non-linear least squares problem between the forward model $\varepsilon_{pe}(h)$ and the observed volume excitation rate $\tilde{\varepsilon}_{pe}(h)$, i.e.,

$$\chi^2_\mu = \frac{1}{\mu} \sum_h \left(\frac{\tilde{\varepsilon}_{pe}(h) - \varepsilon_{pe}(h)}{\delta(h)} \right)^2, \tag{4}$$

where χ^2_μ is the chi-square value, δ is the standard deviation of each measurement, and μ is the number of degrees of freedom in the fit, which is equal to the number of altitude measurements. The characteristic flux Q_h and characteristic energy E_h as a function of altitude are the parameters that are being fit.

The problem in (4) is underdetermined since the number of unknowns is twice the number of measurements. Thus, there are infinite number of possible solutions. To make the solution unique, additional regularization terms are required. The regularized problem may be written as an optimization problem as

$$\text{minimize: } \chi^2_\mu \tag{5}$$

$$\text{subject to: } r(\mathbf{Q}, \mathbf{E}) > 0 \tag{6}$$

where $\mathbf{Q}$ and $\mathbf{E}$ are the column vectors of Q_h and E_h at different altitudes, respectively. The term r is the regularizer, which is selected based on the physical knowledge of the CPE spectra.

Due to the inelastic collisions of CPEs with neutral particles and thermal electrons, the characteristic energy and characteristic flux decreases with decreasing altitude, i.e., $(E_h - E_{h-1} > 0)$ and $(Q_h - Q_{h-1} > 0)$. This information could be added to the problem as a penalty on the gradient, i.e.,

$$r(\mathbf{Q}, \mathbf{E}) = \lambda_0 \, \|\mathbf{G}\,\mathbf{Q}\|_1 + \lambda_1 \, \|\mathbf{G}\,\mathbf{E}\|_1. \tag{7}$$

where the matrix $\mathbf{G}$ measures the gradient of $\mathbf{Q}$ and $\mathbf{E}$ at consecutive altitudes, $\|.\|_1$ is the l_1-norm, and λ_0 and λ_1 are the tuning parameters, which weight the energy gradient. For simplicity, we use $\lambda = \lambda_0 = \lambda_1 = 1.0$. The solution is not sensitive to λ. Additional physical bounds are added to the problem to speed up the solution process and to constrain the solution to realistic physical ranges, namely, $E_h = [5, 50]\, eV$ and $Q_h = [1e2, 1e12]\, cm^{-2}s^{-1}eV^{-1}$. hola pepe como estas ho lnoaf cjondsf

5 Experimental results

We now present preliminary results of CPE energy spectra inversion from coincident ICON-FUV and COSMIC2 observations in the nighttime ionosphere. Figure 2(a) shows the ICON satellite's location, the ICON-FUV's line of sight, and the ionospheric pierce point of ICON and COSMIC2 on 04/01/2020 at 11:09:19UTC (SZA=113°). The spatial separation between pierce points is less than 4° in both latitude and longitude, and less than 15 min in time (criteria for coincident observations). The ICON-FUV's line of sight and its conjugate trace are included for determining what percent of the latter is sunlit. When the conjugate trace is in the darkness, VERs estimated from ICON-FUV and COSMIC2 are expected to be similar. However, when the conjugate trace is completely sunlit, the VER observed by ICON might be up to one order of magnitude higher than that observed by COSMIC2.

Figure 2(b) shows the source VER (ε_0) observed by ICON (red) and the VER due to RR + MN (ε_{rr}+ε_{mn}) calculated from COSMIC2 observations (blue) for the selected example. The volume excitation rate due to PE impact $\tilde{\varepsilon}_{pe}$ calculated using (1) is also shown (green). CPEs dominate the production of FUV airglow in this case. During the winter solstice (January 2020) in the nighttime, 35% of ICON-FUV data was affected by CPEs.

Figure 2(c) shows the geographical distribution of coincident measurements by ICON and COSMIC2 during Jan/Feb 2020, and 2(d) shows the VER difference calculated from ICON-FUV and COSMIC2 as a function of the percent of the conjugate trace in sunlit conditions, hereafter the sunlit conjugate. Figure 2(d) shows an explicit dependency between what ICON-FUV and COSMIC observe, and the sunlit conjugate. In average, the amount of airglow due to PE impact exceeds that due to MN and RR by ~ 0.55 ph/cm^3 when the FUV's conjugate trace is completely illuminated.

Since VERs from ICON-FUV measurements are determined assuming a homogeneous ionosphere, estimates when the conjugate trace is partially illuminated might lead to miscalculations. Therefore, we only use measurements when the conjugate trace is completely illuminated to invert the PE energy spectra.

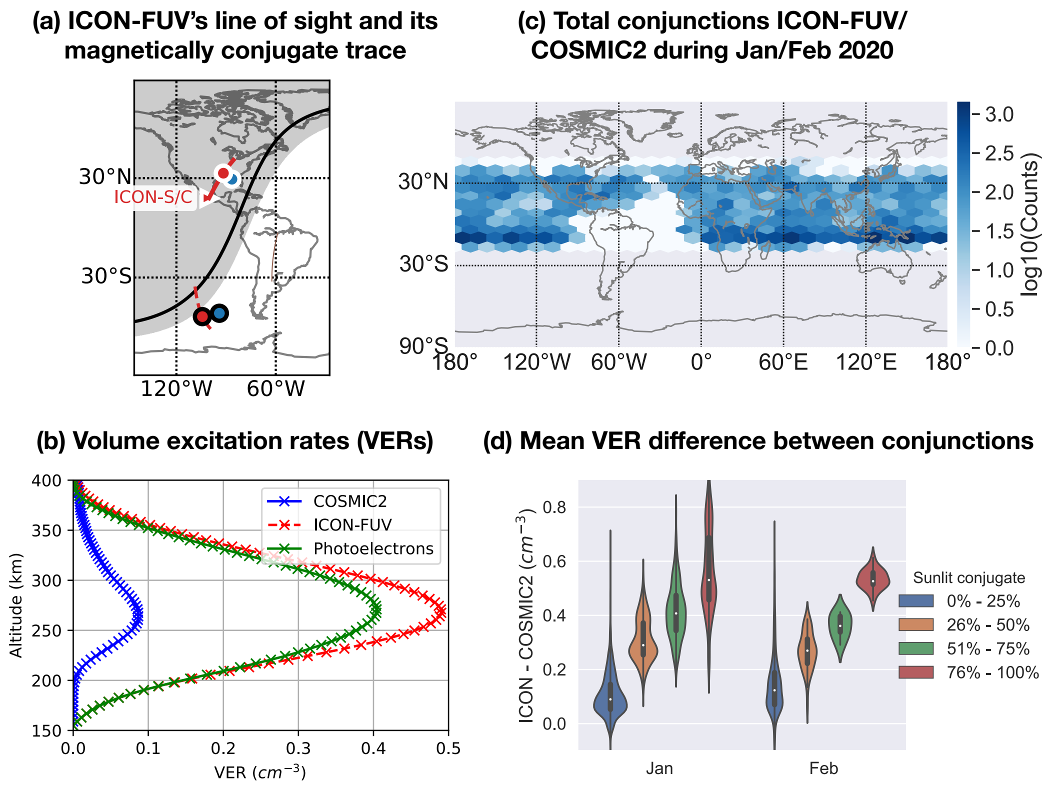

Figure 2. Coincident measurements of volume excitation rates from ICON-FUV and COSMIC2. (a) The ICON and COSMIC2 satellite's location on 04/01/2020 at 11:09:19UTC are shown in red and blue, respectively. The FUV's line of sight at the peak height (∼270km) and its magnetically conjugate trace are shown by solid and dashed red lines, respectively. Besides the night/day side at the sea level, the terminator at 300km altitude is indicated by the solid black line (b) the VER measured by ICON-FUV (red), the VER calculation due to RR and MN (blue) inferred from COSMIC2, and the VER difference associated with PE impact (green) for the same time as (a). (c) Geographical distribution of total coincidences ICON/COSMIC2 during Jan/Feb 2020 (d) Mean VER difference between ICON/COSMIC2 coincident observations as a function of the percent of the ICON's conjugate trace in sun light.

Estimates of the PE energy spectra are shown in Figure 3(a) for the same example shown in Figure 2. This spectra was estimated making use of the measured $\tilde{\varepsilon}_{pe}$ and solving (6) using the numpy Sequential Least SQuares Programming (SLSQP) algorithm (Kraft, 1988). Other non-linear minimizers provided similar results, but the SLSQP algorithm was selected because of its speed and versatility in managing any combination of bounds, equality, and inequality constraints.

The estimated PE flux shown in 3(a) decreases slightly with decreasing altitude until the peak height, where the PE flux begins to fall rapidly. At 200km, the PE flux is almost one order of magnitude less than the one at 270km, which is consistent with its corresponding volume excitation rate due to PE impact shown in Figure 2(b).

The difference in the PE flux above and below the peak height can be explained by their dominant processes. Above the peak height, the amount of PEs barely varies since there is no local production or losses due to interactions with neutrals or thermal electrons. Whereas, below the peak height, the PEs are rapidly losing their energy due to collisions with neutrals and thermal electrons.

6 Comparisons with SAMI2-PE outputs

SAMI2-PE is a 2D model (Varney et al., 2012) based on the SAMI2 model (Huba et al., 2000). SAMI2 uses a photoelectron heating model developed by Swartz and Nisbet (1972) in which the electron heating is deposited locally below 300km with an efficiency factor proportional to the O^+ photoionization rate, and an exponential decay dependence above 300km along the magnetic field line. However, Varney et al. (2011) noted the limitations of this model in comparing SAMI2 electron temperature results to Jicamarca data. Subsequently, SAMI2-PE was developed to improve SAMI2 by incorporating a physics-based photoelectron transport model to compute electron heating rates and secondary photo production ionization rates. A multi-stream transport equation (Schunk & Nagy, 2009) is used to calculate the photoelectron flux including transport, elastic and inelastic collisions, and energy transfer to the ambient electrons.

SAMI2 and SAMI2-PE make no calculations of the major neutral species, these and neutral winds must be provided as inputs to the model. Neutral species and neutral winds are specified using the empirical models NRL-MSISE00 (Picone et al., 2002) and HWM93 (Hedin et al., 1991), respectively. Since there is evidence that NRL-MSISE00 overestimates the [O] density during solar minimum conditions by 20% (Meier et al., 2015; Shepherd et al., 2016), the [O] density was scaled by a factor of 0.8. Other input specifications in SAMI2-PE are the number of altitudes, grid cells, energy bins, and pitch angles. For this work, we used 90, 151, 103, and 8, respectively.

The PE flux from SAMI2-PE for the same time and location of the reference is shown in Figure 3(b). Comparing both PE fluxes, their morphologies show a remarkable agreement above the F peak, although the SAMI2-PE output is ∼10% higher. Similar comparisons at low latitudes show a lower difference (∼4%). Below the F peak there is a notable discrepancy between the estimated and modeled PE flux. While the estimated PE flux is considerably reduced at 200km (one order of magnitude less), the modeled is not. Comparisons of SAMI2-PE outputs with ISR measurements at Jicamarca have also shown discrepancies below the F peak of electron temperatures and densities. According to Varney et al. (2012), in this altitude regime, the cooling rates might be either too low, the recombination rates too high, or extra production terms might have been neglected. This might explain the differences observed between the estimated and the modeled PE flux. More comprehensive analyses would be the subject of future studies.

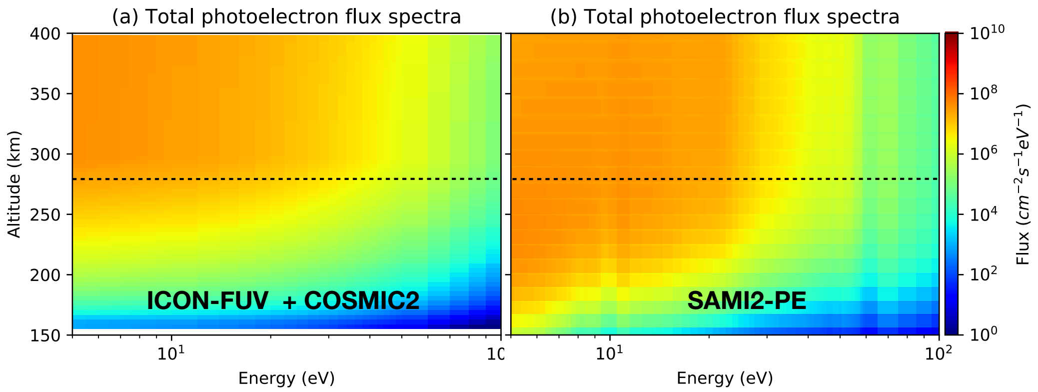

Figure 3. Total photoelectron flux as a function of energy and altitude at 31°N, 91°W on 04/01/2020 at 11:09:19UTC. (a) Estimates using the proposed method and (b) SAMI2-PE outputs.

7 Uncertainties

In the previous section, we demonstrated our method's ability to estimate PE energy spectra from FUV and RO measurements. We now discuss potential sources of uncertainties of our proposed method. They are: (1) the neutral atmosphere model, and (2) the observing geometry and time resolution of FUV and RO measurements.

While it is difficult to quantify precisely the error introduced by the neutral atmosphere model, there is evidence that the NRL-MSIS00 model does not accurately reproduce how low the [O] density become during solar minimum conditions (Meier et al., 2015; Shepherd et al., 2016). In this work, the [O] density was scaled by a factor of 0.8 as suggested by Meier et al. (2015) to obtain the SAMI2-PE outputs and to estimate the VER due to CPE excitation.

As shown in Figure 2(d), even when the conjugate trace is not sunlit, there is a small but consistent difference between VERs estimated from ICON-FUV and COSMIC2. This difference is primarily attributed to the observing volume since the spatial and temporal resolution of ICON and COSMIC2 are not identical. The spatial resolution of ICON-FUV is $\sim 3°$ in the horizontal direction and 0.093° in the vertical, compared to $\sim 15°$ and 10° of COSMIC2. The time resolution of FUV and COSMIC2 is 12s and 5-10min, respectively. Such differences are important when the ionosphere is not horizontally homogeneous, e.g., when observing the Equatorial Anomaly. From our data, we can calculate the maximum relative error introduced by these differences to the PE flux estimation comparing the VER difference between ICON and COSMIC2 when the sunlit conjugate is 0% and 100%, which results in a maximum error of $\sim 12\%$.

8 Summary and Conclusions

We presented a method for determining incoming PE fluxes as a function of energy and altitude by combining global scale FUV and RO measurements. By using ICON-FUV and COSMIC-2 measurements, we demonstrated the capability of the proposed technique and examined its validity to characterize CPE spectra. Such characterization provides important insight to the understanding of CPE, its temporal and geographical distribution which impacts the ICON observations.

Through an extensive analysis of ICON-COSMIC2 conjunctions during Jan-Jul 2020, we found that a considerable amount (∼35%) of ICON-FUV nighttime measurements were affected by CPEs during the December solstice in the Northern hemisphere. During other periods (Mar-Jul), the amount of nighttime data affected by CPEs was less than 5%, which is mainly explained by: (1) ICON mostly observes the northern hemisphere, and (2) In the northern hemisphere, CPE airglow is not favored during the June solstice, or close to it, due to the orientation of solar illumination respect to the magnetic field lines. The geographical and temporal distribution of ICON-FUV measurements affected by CPEs closely coincide with that reported by Kil et al. (2020) using the SUSSI FUV instrument. Note that they did not quantify the CPE contribution.

Finally, we compared our estimates with a model based on first principles, SAMI2-PE. Our comparisons show a remarkable agreement at low/mid latitudes (<10%) and altitudes above the peak height. Below the peak height, some discrepancies are observed which might be attributed to some missing production terms in the model.

Acknowledgments

This research was supported by the NASA's Explorers Program under the Ionospheric CONnection Explorer (ICON) project contract number NNG12FA45C, and partially supported by the NASA's grants NNG12FA42I, and 80NSSC20K0706 (JDH). All ICON-FUV, COSMIC2, and GOLD data used in this work are available from https://icon.ssl.berkeley.edu/, https://www.cosmic.ucar.edu/, and https://gold.cs.ucf.edu/, respectively. The SAMI2-PE model outputs are available from https://doi.org/10.13012/B2IDB-2215727_V1 (not yet available, data included as supplement for review purposes).

References

Anthes, R. A., & Schreiner, W. (2019, 8). Six New Satellites Watch the Atmosphere over Earth's Equator. *Eos*, *100*. Retrieved from `https://eos.org/science-updates/six-new-satellites-watch-the-atmosphere-over-earths-equator` doi: 10.1029/2019EO131779

Bailey, G. J., & Balan, N. (1996). A low-latitude ionosphere-plasmasphere model. In R. W. Schunk (Ed.), *Solar terrestrial energy program: Handbook on ionospheric models* (pp. 173–206). Logan: Utah State Univ.

Banks, P. M., Chappell, C. R., & Nagy, A. F. (1974, 4). A new model for the interaction of auroral electrons with the atmosphere: Spectral degradation, backscatter, optical emission, and ionization. *Journal of Geophysical Research*, *79*(10), 1459–1470. Retrieved from `https://agupubs.onlinelibrary.wiley.com/doi/10.1029/JA079i010p01459` doi: 10.1029/ja079i010p01459

Bennett, R. T. (1969, 1). Latitude dependence of 6300 A (O I) twilight airglow enhancement. *Journal of Geophysical Research*, *74*(1), 381–383. doi: 10.1029/ja074i001p00381

Carlson, H. C. (1966, 1). Ionospheric heating by magnetic conjugate-point photoelectrons. *Journal of Geophysical Research*, *71*(1), 195–199. Retrieved from `https://agupubs.onlinelibrary.wiley.com/doi/10.1029/JZ071i001p00195` doi: 10.1029/JZ071i001p00195

Carlson, H. C. (1968, 7). Most Recent Studies of Low Latitude Effects Due to Conjugate Location Heating. *Radio Science*, *3*(7), 668–673. Retrieved from `http://doi.wiley.com/10.1002/rds196837668` doi: 10.1002/rds196837668

Carman, E. H., Hatzopoulos, G. J., & Heeran, M. P. (1969, 9). Predawn enhancement of 6300 Å airglow in conjugate regions. *Planetary and Space Science*, *17*(9), 1677–1679. doi: 10.1016/0032-0633(69)90155-x

Christensen, A. B. (1975, 5). Observations of OI 7774 emission excited by conjugate photoelectrons. *Planetary and Space Science*, *23*(5), 831–842. Retrieved from `https://linkinghub.elsevier.com/retrieve/pii/0032063375900203` doi:

10.1016/0032-0633(75)90020-3

Christensen, A. B., Walterscheid, R. L., Ross, M. N., Meng, C.-I., Paxton, L. J., Anderson, D. E., Jr., ... Strickland, D. J. (1994, 9). Global Ultraviolet Imager (GUVI) for the NASA Thermosphere-Ionsphere-Mesosphere Energetics and Dynamics (TIMED) mission. In J. Wang & P. B. Hays (Eds.), *Optical spectroscopic techniques and instrumentation for atmospheric and space research* (p. 451). Retrieved from `http://proceedings.spiedigitallibrary.org/proceeding.aspx?doi=10.1117/12.366380http://proceedings.spiedigitallibrary.org/proceeding.aspx?doi=10.1117/12.187583` doi: 10.1117/12.187583

Cogger, L. L., & Shepherd, G. G. (1969, 11). Observations of a magnetic conjugate effect in the OI 6300 Å airglow at Saskatoon. *Planetary and Space Science*, *17*(11), 1857–1865. doi: 10.1016/0032-0633(69)90160-3

Cole, K. D. (1965). The predawn enhancement of 6300Å airglow. *Annales Geophysicae*, *21*(156), 196.

Comberiate, J. M., Kamalabadi, F., & Paxton, L. J. (2007, 4). A tomographic model for ionospheric imaging with the global ultraviolet imager. *Radio Science*, *42*(2), n/a-n/a. Retrieved from `https://agupubs.onlinelibrary.wiley.com/doi/10.1029/2005RS003348` doi: 10.1029/2005RS003348

Duboin, M. L., Lejeune, G., Petit, M., & Weill, G. (1968). Excitation of the oxygen lines and ionospheric heating by conjugate photoelectrons. *Journal of Atmospheric and Terrestrial Physics*, *30*(2), 299–304. Retrieved from `https://ui.adsabs.harvard.edu/abs/1968JATP...30..299D/abstract` doi: 10.1016/0021-9169(68)90084-6

Eastes, R. W., McClintock, W. E., Burns, A. G., Anderson, D. N., Andersson, L., Codrescu, M., ... Oberheide, J. (2017, 10). The Global-Scale Observations of the Limb and Disk (GOLD) Mission. *Space Science Reviews*, *212*(1-2), 383–408. Retrieved from `https://link.springer.com/article/10.1007/s11214-017-0392-2http://link.springer.com/10.1007/s11214-017-0392-2` doi: 10.1007/s11214-017-0392-2

Eastes, R. W., McClintock, W. E., Codrescu, M. V., Aksnes, A., Anderson, D. N., Andersson, L., ... Woods, T. N. (2008). Global-Scale Observations of the Limb and Disk (GOLD): New observing capabilities for the ionosphere-thermosphere. In *Geophysical monograph series* (Vol. 181, pp. 319–326). Blackwell Publishing Ltd. Retrieved from `http://www.agu.org/books/gm/v181/181GM29/181GM29.shtml` doi: 10.1029/181GM29

Evans, J. V. (1967, 10). Midlatitude electron and ion temperatures at sunspot minimum. *Planetary and Space Science*, *15*(10), 1557–1570. doi: 10.1016/0032-0633(67)90089-x

Fontheim, E. G., Beutler, A. E., & Nagy, A. F. (1968). Theoretical calculations of the conjugate predawn effects. *Annales Geophysicae*, *24*, 489.

Hanson, W. B. (1963). Electron Temperatures in the Upper Atmosphere. *Space Res.*, *3*, 282. Retrieved from `https://ui.adsabs.harvard.edu/abs/1963spre.conf..282H/abstract`

Hanson, W. B. (1969, 7). Radiative recombination of atomic oxygen ions in the nighttime F region. *Journal of Geophysical Research*, *74*(14), 3720–3722. Retrieved from `https://agupubs.onlinelibrary.wiley.com/doi/10.1029/JA074i014p03720` doi: 10.1029/JA074i014p03720

Hanson, W. B. (1970, 8). A comparison of the oxygen ion-ion neutralization and radiative recombination mechanisms for producing the ultraviolet nightglow. *Journal of Geophysical Research*, *75*(22), 4343–4346. Retrieved from `http://doi.wiley.com/10.1029/JA075i022p04343` doi: 10.1029/JA075i022p04343

Hays, P. B., & Sharp, W. E. (1973, 3). Twilight airglow: 1. Photoelectrons and [O I] 5577-Angstrom radiation. *Journal of Geophysical Research*, *78*(7), 1153–

1166. Retrieved from https://agupubs.onlinelibrary.wiley.com/doi/10.1029/JA078i007p01153 doi: 10.1029/ja078i007p01153

Hedin, A. E., Biondi, M. A., Burnside, R. G., Hernandez, G., Johnson, R. M., Killeen, T. L., … Virdi, T. S. (1991, 5). Revised global model of thermosphere winds using satellite and ground-based observations. *Journal of Geophysical Research*, *96*(A5), 7657. Retrieved from http://doi.wiley.com/10.1029/91JA00251 doi: 10.1029/91JA00251

Huba, J. D., Joyce, G., & Fedder, J. A. (2000, 10). Sami2 is Another Model of the Ionosphere (SAMI2): A new low-latitude ionosphere model. *Journal of Geophysical Research: Space Physics*, *105*(A10), 23035–23053. Retrieved from http://doi.wiley.com/10.1029/2000JA000035 doi: 10.1029/2000JA000035

Immel, T. J., England, S. L., Mende, S. B., Heelis, R. A., Englert, C. R., Edelstein, J., … Sirk, M. M. (2018, 2). The Ionospheric Connection Explorer Mission: Mission Goals and Design. *Space Science Reviews*, *214*(1), 13. Retrieved from http://link.springer.com/10.1007/s11214-017-0449-2https://link.springer.com/article/10.1007/s11214-017-0449-2 doi: 10.1007/s11214-017-0449-2

Jursa, A. S. (1985). *Handbook of Geophysics and the Space Environment.* San Francisco, CAL: Air Force Geophysics Laboratory Hanscom.

Kaeppler, S. R., Hampton, D. L., Nicolls, M. J., Strømme, A., Solomon, S. C., Hecht, J. H., & Conde, M. G. (2015, 10). An investigation comparing ground-based techniques that quantify auroral electron flux and conductance. *Journal of Geophysical Research: Space Physics*, *120*(10), 9038–9056. Retrieved from http://doi.wiley.com/10.1002/2015JA021396 doi: 10.1002/2015JA021396

Kamalabadi, F., Bust, G., Dymond, K., Gonzalez, S., Bernhardt, P., Chakrabarti, S., … Thonnard, S. (2002, 8). Tomographic studies of aeronomic phenomena using radio and UV techniques. *Journal of Atmospheric and Solar-Terrestrial Physics*, *64*(12-14), 1573–1580. Retrieved from https://linkinghub.elsevier.com/retrieve/pii/S1364682602000962 doi: 10.1016/S1364-6826(02)00096-2

Kamalabadi, F., Comberiate, J. M., Taylor, M. J., & Pautet, P. D. (2009, 6). Estimation of electron densities in the lower thermosphere from GUVI 135.6 nm tomographic inversions in support of SpreadFEx. *Annales Geophysicae*, *27*(6), 2439–2448. Retrieved from https://angeo.copernicus.org/articles/27/2439/2009/ doi: 10.5194/angeo-27-2439-2009

Kamalabadi, F., Karl, W. C., Semeter, J. L., Cotton, D. M., Cook, T. A., & Chakrabarti, S. (1999, 3). A statistical framework for space-based EUV ionospheric tomography. *Radio Science*, *34*(2), 437–447. Retrieved from http://doi.wiley.com/10.1029/1998RS900026 doi: 10.1029/1998RS900026

Kamalabadi, F., Qin, J., Harding, B. J., Iliou, D., Makela, J. J., Meier, R. R., … Immel, T. J. (2018, 6). Inferring nighttime ionospheric parameters with the far ultraviolet imager onboard the ionospheric connection explorer. *Space Science Reviews*, *214*(4), 70. Retrieved from http://link.springer.com/10.1007/s11214-018-0502-9 doi: 10.1007/s11214-018-0502-9

Khazanov, G. V., Glocer, A., & Himwich, E. W. (2014, 1). Magnetosphere-ionosphere energy interchange in the electron diffuse aurora. *Journal of Geophysical Research: Space Physics*, *119*(1), 171–184. Retrieved from http://doi.wiley.com/10.1002/2013JA019325 doi: 10.1002/2013JA019325

Kil, H., Schaefer, R. K., Paxton, L. J., & Jee, G. (2020, 1). The Far Ultraviolet Signatures of Conjugate Photoelectrons Seen by the Special Sensor Ultraviolet Spectrographic Imager. *Geophysical Research Letters*, *47*(1). Retrieved from https://onlinelibrary.wiley.com/doi/abs/10.1029/2019GL086383 doi: 10.1029/2019GL086383

Knudsen, W. C. (1970, 7). Tropical ultraviolet nightglow from oxygen ion-ion neutralization. *Journal of Geophysical Research*, *75*(19), 3862–3866. Retrieved from `http://doi.wiley.com/10.1029/JA075i019p03862` doi: 10.1029/JA075i019p03862

Kondo, Y., & Ogawa, T. (1976). Odd nitrogen in the lower thermosphere under auroral perturbations. *Journal of geomagnetism and geoelectricity*, *28*(4), 253–282. Retrieved from `http://joi.jlc.jst.go.jp/JST.Journalarchive/jgg1949/28.253?from=CrossRef` doi: 10.5636/jgg.28.253

Kraft, D. (1988). *A software package for sequential quadratic programming* (Tech. Rep.). Koln, Germany: DLR German Aerospace Center.

Kuo, Y., Wee, T., Sokolovskiy, S., Rocken, C., Schreiner, W., & Hunt, D. (2004). Inversion and Error Estimation of GPS Radio Occultation Data. *Journal of the Meteorological Society of Japan*, *82*(1B), 507–531. doi: 10.2151/jmsj.2004.507

Lei, J., Syndergaard, S., Burns, A. G., Solomon, S. C., Wang, W., Zeng, Z., ... Lin, C. H. (2007, 7). Comparison of COSMIC ionospheric measurements with ground-based observations and model predictions: Preliminary results. *Journal of Geophysical Research: Space Physics*, *112*(7). doi: 10.1029/2006JA012240

Meier, R. R. (1971, 1). Observations of conjugate excitation of the O I 1304-A airglow. *Journal of Geophysical Research*, *76*(1), 242–247. Retrieved from `http://doi.wiley.com/10.1029/JA076i001p00242` doi: 10.1029/JA076i001p00242

Meier, R. R. (1991, 12). Ultraviolet spectroscopy and remote sensing of the upper atmosphere. *Space Science Reviews*, *58*(1), 1–185. Retrieved from `http://link.springer.com/10.1007/BF01206000` doi: 10.1007/BF01206000

Meier, R. R., Picone, J. M., Drob, D. P., Bishop, J., Emmert, J. T., Lean, J. L., ... Gibson, S. T. (2015, 1). Remote Sensing of Earth's Limb by TIMED/GUVI: Retrieval of thermospheric composition and temperature. *Earth and Space Science*, *2*(1), 1–37. Retrieved from `http://doi.wiley.com/10.1002/2014EA000035` doi: 10.1002/2014EA000035

Mende, S. B., Frey, H. U., Rider, K., Chou, C., Harris, S. E., Siegmund, O. H. W., ... Ellis, S. (2017, 10). The far ultra-violet imager on the icon mission. *Space Science Reviews*, *212*(1-2), 655–696. Retrieved from `http://link.springer.com/10.1007/s11214-017-0386-0` doi: 10.1007/s11214-017-0386-0

Mukai, T., Kondo, Y., & Hirao, K. (1979, 1). Rocket observation of conjugate photoelectrons in the predawn ionosphere. *Planetary and Space Science*, *27*(1), 31–38. doi: 10.1016/0032-0633(79)90144-2

Myers, B., Hamlin, D., & Schoonover, M. (1975, 3). Calculated and observed photoelectron-flux spectra at dawn. *Journal of Atmospheric and Terrestrial Physics*, *37*(3), 387–406. Retrieved from `https://linkinghub.elsevier.com/retrieve/pii/0021916975901695` doi: 10.1016/0021-9169(75)90169-5

Nagy, A. F., & Banks, P. M. (1970, 11). Photoelectron fluxes in the ionosphere. *Journal of Geophysical Research*, *75*(31), 6260–6270. Retrieved from `https://agupubs.onlinelibrary.wiley.com/doi/10.1029/JA075i031p06260` doi: 10.1029/JA075i031p06260

Narasinga Rao, B. C., & Maier, E. J. R. (1970, 2). Photoelectron flux and protonospheric heating during the conjugate point sunrise. *Journal of Geophysical Research*, *75*(4), 816–822. Retrieved from `http://doi.wiley.com/10.1029/JA075i004p00816` doi: 10.1029/JA075i004p00816

Paxton, L. J., Schaefer, R. K., Zhang, Y., & Kil, H. (2017, 2). Far ultraviolet instrument technology. *Journal of Geophysical Research: Space Physics*, *122*(2), 2706–2733. Retrieved from `https://onlinelibrary.wiley.com/doi/abs/10.1002/2016JA023578` doi: 10.1002/2016JA023578

Peterson, W. K., Doering, J. P., Potemra, T. A., McEntire, R. W., & Bostrom, C. O. (1977, 3). Conjugate photoelectron fluxes observed on Atmosphere Explorer C. *Geophysical Research Letters*, *4*(3), 109–112. Retrieved from http://doi.wiley.com/10.1029/GL004i003p00109 doi: 10.1029/GL004i003p00109

Pfaff, R., Carlson, H. C., Watzin, J., Everett, D., & Gruner, T. (2001). *An overview of the Fast Auroral Snapshot (FAST) satellite* (Vol. 98) (No. 1-2). Springer. Retrieved from https://link.springer.com/article/10.1023/A:1013187826070 doi: 10.1023/A:1013187826070

Picone, J. M., Hedin, A. E., Drob, D. P., & Aikin, A. C. (2002, 12). NRLMSISE-00 empirical model of the atmosphere: Statistical comparisons and scientific issues. *Journal of Geophysical Research: Space Physics*, *107*(A12), 15–1. Retrieved from https://agupubs.onlinelibrary.wiley.com/doi/10.1029/2002JA009430 doi: 10.1029/2002JA009430

Qin, J., Makela, J. J., Kamalabadi, F., & Meier, R. R. (2015, 11). Radiative transfer modeling of the OI 135.6 nm emission in the nighttime ionosphere. *Journal of Geophysical Research A: Space Physics*, *120*(11), 10116–10135. doi: 10.1002/2015JA021687

Rees, M. H., & Luckey, D. (1974, 12). Auroral electron energy derived from ratio of spectroscopic emissions 1. Model computations. *Journal of Geophysical Research*, *79*(34), 5181–5186. Retrieved from http://doi.wiley.com/10.1029/JA079i034p05181 doi: 10.1029/JA079i034p05181

Richards, P. G., & Peterson, W. K. (2008, 8). Measured and modeled backscatter of ionospheric photoelectron fluxes. *Journal of Geophysical Research: Space Physics*, *113*(8), 1–13. Retrieved from http://doi.wiley.com/10.1029/2008JA013092 doi: 10.1029/2008JA013092

Richards, P. G., & Torr, D. G. (1990, 7). Auroral modeling of the 3371 Å emission rate: Dependence on characteristic electron energy. *Journal of Geophysical Research*, *95*(A7), 10337. Retrieved from https://agupubs.onlinelibrary.wiley.com/doi/10.1029/JA095iA07p10337http://doi.wiley.com/10.1029/JA095iA07p10337 doi: 10.1029/JA095iA07p10337

Schreiner, W., Rocken, C., Sokolovskiy, S., Syndergaard, S., & Hunt, D. (2007, 2). Estimates of the precision of GPS radio occultations from the COSMIC/FORMOSAT-3 mission. *Geophysical Research Letters*, *34*(4), L04808. Retrieved from http://doi.wiley.com/10.1029/2006GL027557 doi: 10.1029/2006GL027557

Schreiner, W. S., Sokolovskiy, S. V., Rocken, C., & Hunt, D. C. (1999, 7). Analysis and validation of GPS/MET radio occultation data in the ionosphere. *Radio Science*, *34*(4), 949–966. Retrieved from http://doi.wiley.com/10.1029/1999RS900034 doi: 10.1029/1999RS900034

Schreiner, W. S., Weiss, J. P., Anthes, R. A., Braun, J., Chu, V., Fong, J., … Zeng, Z. (2020). COSMIC-2 Radio Occultation Constellation: First Results. *Geophysical Research Letters*, *47*(4), 1–7. doi: 10.1029/2019GL086841

Schunk, R., & Nagy, A. (2009). *Ionospheres: physics, plasma physics, and chemistry.*

Semeter, J., & Kamalabadi, F. (2005, 4). Determination of primary electron spectra from incoherent scatter radar measurements of the auroral E region. *Radio Science*, *40*(2), n/a-n/a. Retrieved from http://doi.wiley.com/10.1029/2004RS003042 doi: 10.1029/2004RS003042

Shepherd, G. G., Cho, Y. M., Fomichev, V. I., & Martynenko, O. V. (2016, 9). Thermospheric atomic oxygen concentrations from WINDII O+(2P-2D) 732 nm emission: Comparisons with the NRLMSISE-00 and C-IAM models and with GUVI observations. *Journal of Atmospheric and Solar-Terrestrial Physics*, *147*, 50–58. Retrieved from http://dx.doi.org/10.1016/j.jastp.2016.06.015 doi: 10.1016/j.jastp.2016.06.015

Shepherd, G. G., Pieau, J. F., Ogawa, T., Tohmatsu, T., Oyama, K., & Watanabe, Y. (1978, 3). Direct measurement of conjugate photoelectrons and predawn 630 nm airglow. *Planetary and Space Science*, *26*(3), 211–217. doi:

10.1016/0032-0633(78)90086-7
Smith, R. W. (1969, 5). Some observations of the predawn enhancement of the red line airglow over Great Britain. *Planetary and Space Science*, *17*(5), 879–888. doi: 10.1016/0032-0633(69)90094-4
Solomon, S. C. (2017). Global modeling of thermospheric airglow in the far ultraviolet. *Journal of Geophysical Research: Space Physics*, *122*(7), 7834–7848. doi: 10.1002/2017JA024314
Solomon, S. C., Andersson, L., Burns, A. G., Eastes, R. W., Martinis, C., McClintock, W. E., & Richmond, A. D. (2020). Global-Scale Observations and Modeling of Far-Ultraviolet Airglow During Twilight. *Journal of Geophysical Research: Space Physics*, *125*(3). doi: 10.1029/2019JA027645
Strickland, D. J., Meier, R. R., Hecht, J. H., Christensen, A. B., Strickland, D. J., & Meier, R. R. (1989, 10). Deducing composition and incident electron spectra from ground-based auroral optical measurements: Variations in oxygen density. *Journal of Geophysical Research*, *94*(A10), 13553. Retrieved from http://doi.wiley.com/10.1029/JA094iA10p13553https://agupubs.onlinelibrary.wiley.com/doi/10.1029/JA094iA10p13527 doi: 10.1029/JA094iA10p13553
Swartz, W. E. (1972). *Electron production, recombination and heating in the F - region of the ionosphere* (Unpublished doctoral dissertation). The Pennsylvania University.
Swartz, W. E., & Nisbet, J. S. (1972, 11). Revised calculations of F region ambient electron heating by photoelectrons. *Journal of Geophysical Research*, *77*(31), 6259–6261. Retrieved from http://doi.wiley.com/10.1029/JA077i031p06259 doi: 10.1029/JA077i031p06259
Syndergaard, S., Kursinski, E. R., Herman, B. M., Lane, E. M., & Flittner, D. E. (2005, 9). A Refractive Index Mapping Operator for Assimilation of Occultation Data. *Monthly Weather Review*, *133*(9), 2650–2668. Retrieved from https://journals.ametsoc.org/mwr/article/133/9/2650/67408/A-Refractive-Index-Mapping-Operator-for doi: 10.1175/MWR3001.1
Tien, J., Okihiro, B. B., Esterhuizen, S., Franklin, G., Meehan, T., Munson, T., ... Young, L. (2012, 2). Next Generation Scalable Spaceborne GNSS Science Receiver. In *Proceedings of the 2012 international technical meeting of the institute of navigation* (pp. 882–914). Retrieved from http://www.ion.org/publications/abstract.cfm?jp=p&articleID=9999
Tinsley, B. A., Christensen, A. B., Bittencourt, J., Gouveia, H., Angreji, P. D., & Takahashi, H. (1973, 3). Excitation of oxygen permitted line emissions in the tropical nightglow. *Journal of Geophysical Research*, *78*(7), 1174–1186. Retrieved from https://agupubs.onlinelibrary.wiley.com/doi/10.1029/JA078i007p01174 doi: 10.1029/JA078i007p01174
Varney, R. H., Kelley, M. C., Nicolls, M. J., Heinselman, C. J., & Collins, R. L. (2011). The electron density dependence of polar mesospheric summer echoes. *Journal of Atmospheric and Solar-Terrestrial Physics*, *73*, 2153–2165.
Varney, R. H., Swartz, W. E., Hysell, D. L., & Huba, J. D. (2012, 6). SAMI2-PE: A model of the ionosphere including multistream interhemispheric photoelectron transport. *Journal of Geophysical Research: Space Physics*, *117*(A6). Retrieved from http://doi.wiley.com/10.1029/2011JA017280 doi: 10.1029/2011JA017280
Waldrop, L. S., Kerr, R., & Richards, P. (2008, 1). Photoelectron impact excitation of OI 8446 Å emission observed from Arecibo Observatory. *Journal of Geophysical Research: Space Physics*, *113*(A1), n/a-n/a. Retrieved from http://doi.wiley.com/10.1029/2007JA012356 doi: 10.1029/2007JA012356
Yue, X., Schreiner, W. S., Kuo, Y. H., Hunt, D. C., & Rocken, C. (2013). GNSS radio occultation technique and space weather monitoring. *26th International Technical Meeting of the Satellite Division of the Institute of Navigation, ION*

GNSS 2013, *3*(September 2013), 2508–2522.
Yue, X., Schreiner, W. S., Pedatella, N., Anthes, R. A., Mannucci, A. J., Straus, P. R., & Liu, J.-Y. (2014, 11). Space Weather Observations by GNSS Radio Occultation: From FORMOSAT-3/COSMIC to FORMOSAT-7/COSMIC-2. *Space Weather*, *12*(11), 616–621. Retrieved from http://doi.wiley.com/10.1002/2014SW001133 doi: 10.1002/2014SW001133